

# Automated Ulcer Detection Method from CT Images for Computer Aided Diagnosis of Crohn's Disease

Masahiro ODA<sup>†a)</sup>, Takayuki KITASAKA<sup>††</sup>, *Members*, Kazuhiro FURUKAWA<sup>†††</sup>, Osamu WATANABE<sup>†††</sup>, Takafumi ANDO<sup>†††</sup>, Hidemi GOTO<sup>†††</sup>, *Nonmembers*, and Kensaku MORI<sup>††††</sup>, *Senior Member*

**SUMMARY** Crohn's disease commonly affects the small and large intestines. Its symptoms include ulcers and intestinal stenosis, and its diagnosis is currently performed using an endoscope. However, because the endoscope cannot pass through the stenosed parts of the intestines, diagnosis of the entire intestines is difficult. A CT image-based method is expected to become an alternative way for the diagnosis of Crohn's disease because it enables observation of the entire intestine even if stenosis exists. To achieve efficient CT image-based diagnosis, diagnostic-aid by computers is required. This paper presents an automated detection method of the surface of ulcers in the small and large intestines from fecal tagging CT images. Ulcers cause rough surfaces on the intestinal wall and consist of small convex and concave (CC) regions. We detect them by blob and inverse-blob structure enhancement filters. A roughness value is utilized to reduce the false positives of the detection results. Many CC regions are concentrated in ulcers. The roughness value evaluates the concentration ratio of the detected regions. Detected regions with low roughness values are removed by a thresholding process. The thickness of the intestinal lumen and the CT values of the surrounding tissue of the intestinal lumen are also used to reduce false positives. Experimental results using ten cases of CT images showed that our proposed method detects 70.6% of ulcers with 12.7 FPs/case. The proposed method detected most of the ulcers.

**key words:** ulcer, small and large intestines, detection, computer aided diagnosis, CT image

## 1. Introduction

The number of people suffering from Crohn's disease, an inflammatory disease of the digestive tract, is increasing in Japan [1]. It occurs more often among people living in cities, in developed countries, and in their 20s and 30s [2]. However, its pathogenic mechanism remains unclarified. Crohn's disease commonly affects the small intestine, but it can affect any area of the digestive tract. Its symptoms include ulcers, intestinal stenosis, and fistulae.

Fiber or capsule endoscopic diagnosis is commonly performed in small intestine examinations [3], [4]. A fiber endoscope is inserted into the small intestine through the anus or the mouth. However, these endoscopes cannot pass through the intestine's stenosed parts, which are commonly

caused by Crohn's disease. In such cases, diagnosis of the entire intestine is difficult. Hence, fiber or capsule endoscopic diagnosis is unsuitable.

X-ray CT or MRI-based diagnosis methods of Crohn's disease are receiving attention as alternative diagnostic methods. Such CT or MRI-based diagnosis allows a physician to observe the entire intestine even if intestinal stenosis exists. Several researches related to CT or MRI-based diagnosis of Crohn's disease have been proposed [5]–[14]. Lee et al. compared the detection accuracy of Crohn's disease on CT and MR enterography and small-bowel follow-through examinations [5]. CT and MR enterography utilize 2D CT and MR images for diagnosis. Furukawa et al. reviewed the effects of preparations, contrast agents, and scanning techniques for CT and MR image-based diagnosis [6]. Many researches use MR images for diagnosis [7]–[9]. Several reports related to CT image-based diagnosis have also been reported [8], [10]–[12]. However, most previous researches are based on 2-dimensional (2D) image observation [5]–[12]. Because the shape of the intestine is quite complicated, its 2D image-based diagnosis is difficult and time-consuming. Commercially available CT colonography computer-aided diagnosis (CAD) systems are applicable for Crohn's disease diagnosis and commonly display 3D images to observe the intestine. Ota et al. and Biancone et al. utilized a CT colonography CAD system for Crohn's disease diagnosis [13], [14]. However, the shape of the small intestine is much more complex than the large intestine. Understanding the shapes of the intestine and the lesion positions in it is difficult. Diagnosis of Crohn's disease remains time-consuming even if CT colonography CAD systems are applied. Diagnostic aid based on computer processing is necessary for CT or MRI-based Crohn's disease diagnosis. Automated lesion detection for the symptoms of Crohn's disease is required for efficient diagnosis. To the best of our knowledge, there is no automated ulcer detection method from CT images except our work.

We propose an automated detection method of ulcers inside the intestine, because their presence is one of the symptoms of Crohn's disease. Our fully automated method detects ulcers from 3D abdominal CT images. The surfaces of the internal wall of the intestine are rougher near the ulcers than the normal areas. Figure 1 shows examples of ulcers. The roughed ulcer surfaces consist of convex and concave regions. The size of each convex or concave region is about 2.0 to 5.0 [mm] in diameter. We detect the ulcers

Manuscript received June 19, 2012.

Manuscript revised October 26, 2012.

<sup>†</sup>The author is with the Graduate School of Information Science, Nagoya University, Nagoya-shi, 464–8603 Japan.

<sup>††</sup>The author is with the School of Information Science, Aichi Institute of Technology, Toyota-shi, 470–0392 Japan.

<sup>†††</sup>The authors are with Nagoya University Graduate School of Medicine, Nagoya-shi, 466–8550 Japan.

<sup>††††</sup>The author is with Information and Communications Headquarters, Nagoya University, Nagoya-shi, 464–8601 Japan.

a) E-mail: moda@mori.m.is.nagoya-u.ac.jp

DOI: 10.1587/transinf.E96.D.808

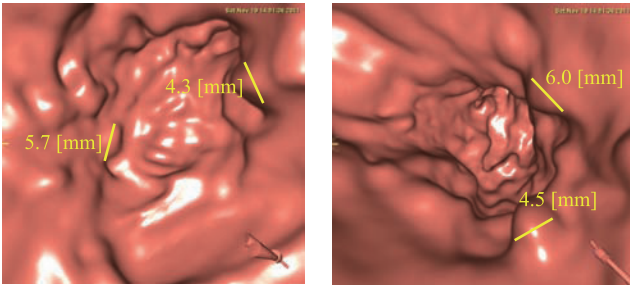


**Fig. 1** Examples of ulcers on intestinal wall shown in virtual endoscopic views. A number of convex and concave regions consist of the rough surface of the ulcer. Each convex and concave region is about 2.0 to 5.0 [mm] in diameter. Sizes of convex regions are overlaid.

using their surface shape features. The convex and concave regions are detected by blob and inverse-blob structure enhancement filters. We utilize a *roughness value* to reduce the false positives (FPs) of the detection results by differentiating between the convex and concave regions concentrated on the rough surface. In ulcer areas, narrowing of the intestinal lumen and thickening of the intestinal wall occur. From this characteristic, we utilize the thickness of the intestinal lumen and the CT values of the surrounding tissue of the intestinal lumen in FP reduction. This is an extended version of a previously proposed ulcer detection method [17].

## 2. Method

### 2.1 Overview

On the intestinal wall, ulcers cause rough surfaces that consist of convex and concave regions. Our proposed method detects these regions by a combination of blob and inverse-blob structure enhancement filters. Many small convex and concave regions are concentrated on the surface of ulcers. This method utilizes the positional correspondences of the convex and concave regions to reduce FPs. The positional correspondences are evaluated by roughness values. We also utilize the thickness of the intestinal lumen and the CT values of the surrounding tissue of the intestinal lumen to reduce FPs. Our method consists of the following processes: intestinal wall region extraction, convex and concave region detection, and FP reduction.

### 2.2 Intestinal Wall Region Extraction

The input of our method is fecal tagging 3D abdominal CT images. We apply an electronic cleansing process based on a previous method [15] to remove the tagged fluid inside the intestines from the input CT images. Figure 2 shows an example of the cleansing result. The resulting CT image of the electronic cleansing process is used in the following processes.

We extract all the voxels inside the body whose CT values are  $a_1$  [H.U.] or less. The small connected components and the lung regions are removed from the extraction result

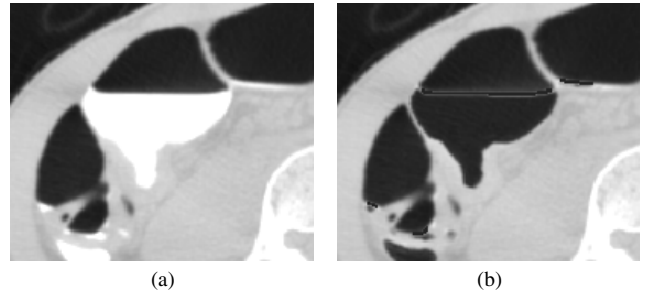


**Fig. 2** Results of electronic cleansing process: (a) original CT image and (b) result of electronic cleansing process.

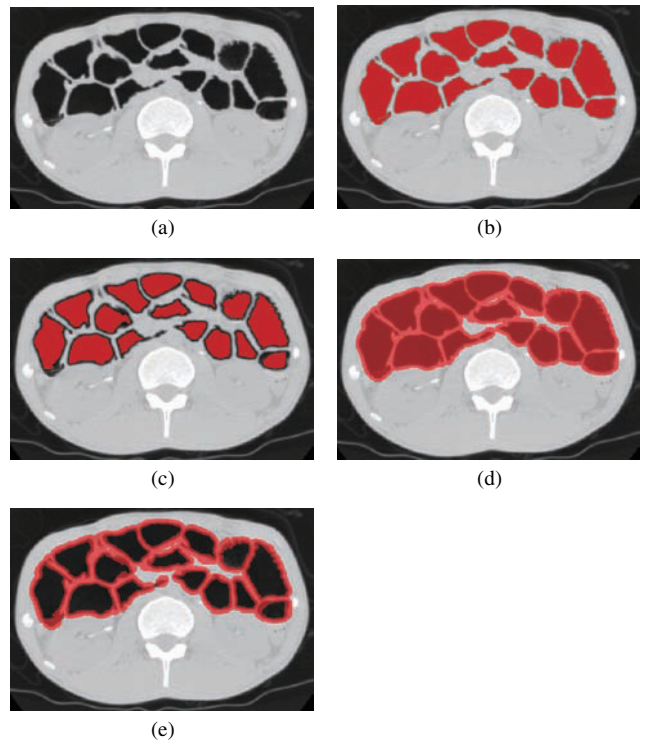


**Fig. 3** Examples of region extraction results: (a) CT image cleansed by electronic cleansing process, (b) air regions  $A_1$ , (c) regions inside intestine  $A_2$ , (d) regions obtained by applying dilation filter to  $A_2$ , and (e) intestinal wall region  $A_3$ .

to eliminate the connected components whose volume are  $a_2$  [mm<sup>3</sup>] or less. The lung region removal eliminates the connected components, which have  $a_3$  [mm<sup>2</sup>] or more area on the axial slice of the most head side.  $a_2$  and  $a_3$  are the threshold values of the volume in a 3D CT image and an area in an axial CT slice, respectively. The remaining regions after these removal processes are defined as air regions  $A_1$  (Fig. 3 (b)).

We obtained the regions inside intestines  $A_2$  by applying an erosion filter to  $A_1$  (Fig. 3 (c)). The structure element of the erosion filter is a sphere of radius  $a_4$  [mm]. Intestinal wall regions  $A_3$  are obtained by subtracting  $A_2$  from the resulting regions of a dilation filter applied to  $A_2$ . The structure element of the dilation filter is a sphere of radius  $a_5$  [mm]. An example of intestinal wall region  $A_3$  is shown

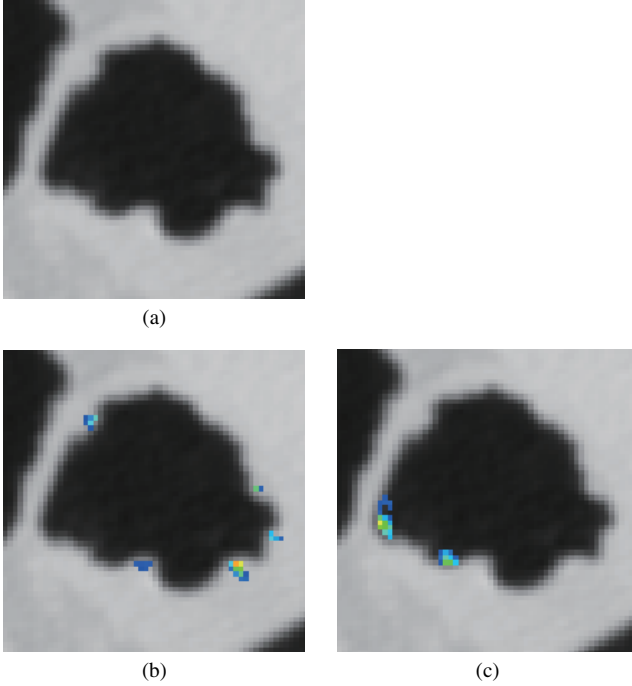


**Fig. 4** (a) Example of convex and concave regions on the intestinal wall. Black regions are air regions. (b) Output values of BSE filter are shown in intestinal wall region. (c) Output values of iBSE filter are shown in air region. In (b) and (c), blue and yellow indicate low and high output values, respectively.

in Fig. 3 (e).

### 2.3 Convex and Concave Region Detection

Ulcers cause convex and concave regions on the internal wall of the intestines. We detect them using two kinds of filters. The CT values inside the convex regions tend to gradually increase from outward to inward; the CT values inside the concave regions tend to gradually decrease from outward to inward. We detect them with intense structures by blob structure enhancement (BSE) and inverse-blob structure enhancement (iBSE) filters [16]. Figure 4 (a) shows examples of the intensity structures of the convex and concave regions.

We approximate the local intensity structures on the CT images by a quadratic polynomial in three variables:

$$f(x, y, z; \mathbf{b}) = b_1x^2 + b_2y^2 + b_3z^2 + b_4xy + b_5yz + b_6zx + b_7x + b_8y + b_9z + b_{10}. \quad (1)$$

We fit it to the neighborhood region of each voxel in  $A_3$ , where  $\mathbf{b} = (b_1, \dots, b_{10})$ . The neighborhood area is a cubic region whose edge length is  $a_6$  [mm]. Coefficient  $\mathbf{b}$  is determined by minimizing the square error of the approximation. The size of a detection target is specified by  $a_6$  [mm]. We set suitable sizes to parameter  $a_6$  to detect 2.0 to 5.0 [mm] of the convex and concave regions and obtain a Hessian matrix

$$\mathbf{H} = \begin{bmatrix} \frac{\partial^2 f}{\partial x^2} & \frac{\partial^2 f}{\partial x \partial y} & \frac{\partial^2 f}{\partial x \partial z} \\ \frac{\partial^2 f}{\partial y \partial x} & \frac{\partial^2 f}{\partial y^2} & \frac{\partial^2 f}{\partial y \partial z} \\ \frac{\partial^2 f}{\partial z \partial x} & \frac{\partial^2 f}{\partial z \partial y} & \frac{\partial^2 f}{\partial z^2} \end{bmatrix}, \quad (2)$$

which consists of the second-order partial differential coefficients of  $f$ . Let the eigenvalues of the Hessian matrix be  $\lambda_1, \lambda_2$ , and  $\lambda_3$  ( $\lambda_1 \geq \lambda_2 \geq \lambda_3$ ). The convex regions on the intestinal wall are detected by the BSE filter, defined as

$$S^1(\lambda_1, \lambda_2, \lambda_3) = \begin{cases} \left[ \frac{\lambda_1^2}{\hat{\lambda}} \right] & \text{if } 0 > \lambda_1, \lambda_2, \lambda_3, \\ 0 & \text{otherwise,} \end{cases} \quad (3)$$

where  $\hat{\lambda} = |\lambda_1 + \lambda_2 + \lambda_3|/3$ . The output values of filter  $S^1$  are shown in Fig. 4 (b). The concave regions are detected by the iBSE filter, defined as

$$S^2(\lambda_1, \lambda_2, \lambda_3) = \begin{cases} \left[ \frac{\lambda_1^2}{\hat{\lambda}} \right] & \text{if } 0 < \lambda_1, \lambda_2, \lambda_3, \\ 0 & \text{otherwise.} \end{cases} \quad (4)$$

An example of the output values of filter  $S^2$  is shown in Fig. 4 (c). BSE filter  $S^1$  and iBSE filter  $S^2$  are used to detect the convex and concave regions on the intestinal wall. The output values of  $S^1$  applied to each voxel in  $A_3$  are stored in convex enhanced image  $I_{1e}$ . Similarly, the output values of  $S^2$  are stored in concave enhanced image  $I_{2e}$ .

## 2.4 FP Reduction

### 2.4.1 Overview

We remove the FPs in the two enhanced images using simple FP reduction processes based on voxel values. The convex and concave candidate regions are obtained from the FP reduction results. We propose three feature values of the convex and concave candidate regions including the roughness value, which evaluates the concentration ratio of the convex and concave candidate regions. The other two feature values are calculated based on the thickness of the intestines and the CT values of the surrounding tissue of the intestines. The FPs of the convex and concave candidate regions are removed by the thresholding processes of the three feature values.

### 2.4.2 Generation of Convex and Concave Candidate Regions

We remove the FPs in enhanced images  $I_{1e}$  and  $I_{2e}$  using thresholding based on the voxel value and the maximum voxel value of the connected components. All voxels with values lower than  $a_7$  are removed from  $I_{1e}$  and  $I_{2e}$ . All connected components where the maximum voxel value in the connected component is smaller than  $a_8$  are removed from  $I_{1e}$ . Similarly, all connected components where the maximum voxel value in the connected component is smaller than  $a_9$  are removed from  $I_{2e}$ .  $a_7$  is a threshold value of a voxel value in the enhanced images.  $a_8$  and  $a_9$  are the threshold values of a maximum voxel value in a connected component. After these simple FP reduction processes, we generate an enhanced image,

$$I_e(x, y, z) = \max(I_{1e}(x, y, z), I_{2e}(x, y, z)), \quad (5)$$

which has a larger value than either  $I_{1e}$  or  $I_{2e}$  on each voxel.  $x$ ,  $y$ , and  $z$  are the coordinates on the enhanced images. The convex and concave candidate regions, which are a set of voxels whose values exceed 1 on enhanced image  $I_e$ , are described as  $c_i$  ( $i = 1, \dots, I$ ).  $i$  and  $I$  are the index and the total number of convex and concave candidate regions, respectively.

### 2.4.3 Roughness Value

Roughness value differentiates the convex and concave regions that are concentrated on the roughed surface from the other convex and concave regions on the internal wall of the intestine. The roughness value is calculated for each  $c_i$ , defined as

$$r_i = \frac{1}{I-1} \sum_{j=1}^I \left( \frac{1}{\rho_1(\mathbf{g}_i - n\mathbf{f}_i, \mathbf{g}_j - n\mathbf{f}_j)} \right)^{R_1} \left( \frac{m}{\rho_2(\mathbf{g}_i - n\mathbf{f}_i, \mathbf{g}_j - n\mathbf{f}_j)} \right)^{R_2} \left( \frac{m}{\rho_3(\mathbf{g}_i - n\mathbf{f}_i, \mathbf{g}_j - n\mathbf{f}_j)} \right)^{R_3} \left( \frac{v_i}{V} \right)^{R_4}, \quad (6)$$

where  $j$  ( $j = 1, \dots, I; j \neq i$ ) is the index of the candidate region,  $\mathbf{g}_i$  is the median point of  $c_i$ ,  $\mathbf{f}_i$  is the average gradient unit vector of the CT values in  $c_i$ ,  $m$  is the weight of the terms,  $n$  is the coefficient of  $\mathbf{f}_i$ ,  $v_i$  is the maximum voxel value in  $c_i$  on the enhanced image, and  $V$  is the maximum value of  $v_i$ .  $R_1, R_2, R_3$ , and  $R_4$  control the sharpnesses of the values of the distance, the average CT value, the maximum CT value, and the maximum voxel value terms, respectively. The roughness value takes high values if many candidate regions are localized close to  $c_i$  and if the maximum value of the enhanced image in  $c_i$  is high. Function  $\rho_1(\mathbf{o}, \mathbf{p})$  calculates the Euclidian distance between points  $\mathbf{o}$  and  $\mathbf{p}$ . The roughness value becomes high if many candidate regions are concentrated near  $c_i$  by utilizing the inverse of  $\rho_1$ . Functions  $\rho_2(\mathbf{o}, \mathbf{p})$  and  $\rho_3(\mathbf{o}, \mathbf{p})$  calculate the average and maximum CT values of the voxels on a line segment connecting  $\mathbf{o}$  and  $\mathbf{p}$ . Many candidate regions are detected on ulcers in the detection process. A line segment connecting two candidate regions on the same ulcer runs through an air region on the CT image. The CT values of the voxels in the air regions are lower than the other regions. If two candidate regions are separated by an intestinal wall, the line segment connecting them runs through the voxels with high CT values. One of these two candidate regions is probably a FP. The inverse of  $\rho_2$  and  $\rho_3$  takes high values if both  $c_i$  and  $c_j$  are located on the same ulcer.

Median point  $\mathbf{g}_i$  of  $c_i$ , which is detected by the BSE filter, is located in the intestinal wall regions. This point must be located in the air regions to calculate  $\rho_2$  and  $\rho_3$ . We use  $\mathbf{g}_i + k\mathbf{f}_i$  instead of  $\mathbf{g}_i$  for the position of  $c_i$  to calculate  $\rho_2$  and  $\rho_3$ . If  $r_i$  is lower than threshold value  $a_{10}$ , region  $c_i$  is removed in the reduction step described below.

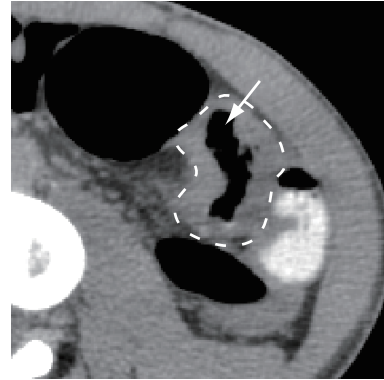


**Fig. 5** Example of narrowed air region in intestine (indicated by an arrow). Narrowed air region is surrounded by thickened intestinal wall. The border between the thickened intestinal wall and the other tissues is shown by a broken line.

### 2.4.4 Thickness of Intestinal Lumen

The thickness of the intestinal wall increases at the lesions including the ulcers. With wall thickening, the air regions in the intestines become narrowed. Figure 5 shows an example of a narrowed air region. We utilize the thickness of the air region in the intestines as a feature value of FP reduction.

We generate a centerline of the small and large intestines with a previous method [18]. The centerline passes through all air regions  $A_1$ . We place points  $\mathbf{p}_k$  ( $k = 1, \dots, K$ ) on the centerline at 0.5 [mm] intervals.  $k$  and  $K$  are the index and the total number of the points on the centerline. For each convex and concave candidate region  $c_i$ , an index of a point on centerline  $\mathbf{p}_{\omega^i}$  closest to  $c_i$  is obtained by

$$\omega^i = \arg \min_k \rho_1(\mathbf{g}_i, \mathbf{p}_k). \quad (7)$$

We apply a distance transformation process to air regions  $A_1$  to calculate the Euclidean distance from the voxels in  $A_1$  to the surrounding tissues.  $h_k$  is the shortest distance from  $\mathbf{p}_k$  to the surrounding tissue of  $A_1$ , which is obtained from the distance transformation result. The average of  $h_k$  is calculated by

$$H = \frac{1}{K} \sum_{k=1}^K h_k. \quad (8)$$

If a convex and concave region is located around narrowed air regions, it probably has a high likelihood of being a part of the ulcers. A distance value at  $\mathbf{p}_{\omega^i}$  is described as  $h_{\omega^i}$ . If it is larger than  $Ha_{11}$ , region  $c_i$  is removed in the reduction step.  $a_{11}$  is a coefficient of the radius of the intestines.

### 2.4.5 CT Values of Surrounding Tissues of Intestinal Lumen

The CT values of the intestinal wall are higher than those of the fat around the intestines. In a normal (non-diseased) area

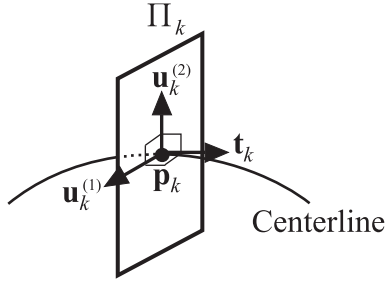


**Fig. 6** Plane located on the centerline of the intestines.  $\mathbf{p}_k$  is a point on the centerline.  $\mathbf{t}_k$  is a tangent vector of it.  $\Pi_k$  is a plane perpendicular to  $\mathbf{t}_k$ .  $\mathbf{u}_k^{(1)}$  and  $\mathbf{u}_k^{(2)}$  are vectors parallel to  $\Pi_k$  and perpendicular to each other.

of the intestines, the intestinal lumen is mainly surrounded by fat because the intestinal wall is very thin. At an ulcerated area of the intestines, the intestinal lumen is surrounded by a thickened intestinal wall. Therefore, the CT values of the tissues around the intestinal lumen are low and high in the normal and ulcerated areas of the intestines. We utilize the CT values of the tissues around the intestinal lumen as a feature value of FP reduction.

We calculate the tangent vector of centerline  $\mathbf{t}_k$  at  $\mathbf{p}_k$  by

$$\mathbf{t}_k = \mathbf{p}_{k+1} - \mathbf{p}_k. \quad (9)$$

Plane  $\Pi_k$ , which is perpendicular to  $\mathbf{t}_k$  and passes through  $\mathbf{p}_k$ , is defined. We cast rays  $\delta_{k,l}$  ( $l = 1, \dots, L$ ) from  $\mathbf{p}_k$  in the direction away from  $\mathbf{p}_k$  on  $\Pi_k$ .  $l$  and  $L$  are the index and the total number of the rays cast on plane  $\Pi_k$ . The direction of ray  $\delta_{k,l}$  is described as

$$\mathbf{d}_{k,l} = \mathbf{u}_k^{(1)} \cos(2\pi l/L) + \mathbf{u}_k^{(2)} \sin(2\pi l/L), \quad (10)$$

where  $\mathbf{u}_k^{(1)}$  and  $\mathbf{u}_k^{(2)}$  are vectors parallel to  $\Pi_k$  and perpendicular to each other. Figure 6 shows their positional relationship. These vectors are calculated by

$$\mathbf{u}_k^{(1)} = \begin{cases} (1, 0, 0) & t_{k,x} = 0 \text{ and } t_{k,y} = 0 \\ \left( \frac{t_{k,y}}{\sqrt{t_{k,x}^2 + t_{k,y}^2}}, \frac{-t_{k,x}}{\sqrt{t_{k,x}^2 + t_{k,y}^2}}, 0 \right) & \text{otherwise} \end{cases} \quad (11)$$

and

$$\mathbf{u}_k^{(2)} = \frac{\mathbf{u}_k^{(1)} \times \mathbf{t}_k}{|\mathbf{u}_k^{(1)} \times \mathbf{t}_k|}, \quad (12)$$

where  $t_{k,x}$ ,  $t_{k,y}$ , and  $t_{k,z}$  are the  $x$ ,  $y$ , and  $z$  components of tangent vector  $\mathbf{t}_k = (t_{k,x}, t_{k,y}, t_{k,z})$ .  $\mathbf{u}_k^{(1)}$  is a vector perpendicular to  $\mathbf{t}_k$  whose  $z$  component is 0.

We define a point on the inner surface of intestines  $\mathbf{w}_{k,l}^{(1)}$  where ray  $\rho_{k,l}$  primarily contacts a voxel having CT values higher than  $a_{12}$  [H.U.]. We also define point  $\mathbf{w}_{k,l}^{(2)}$  where  $a_{13}$  [mm] distant from  $\mathbf{w}_{k,l}^{(1)}$  in ray direction  $\mathbf{d}_{k,l}$ . The positions of  $\mathbf{w}_{k,l}^{(1)}$  and  $\mathbf{w}_{k,l}^{(2)}$  on plane  $\Pi_k$  are outlined in Fig. 7. The average CT value of voxels on a line segment from  $\mathbf{w}_{k,l}^{(1)}$  to  $\mathbf{w}_{k,l}^{(2)}$  is described as  $s_{k,l}$ . The average CT value of the tissue

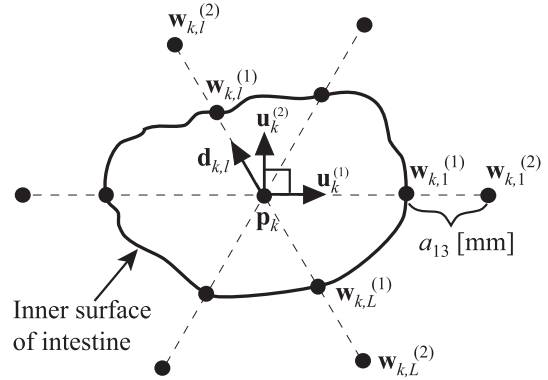


**Fig. 7** Ray directions and points  $\mathbf{w}_{k,l}^{(1)}$  and  $\mathbf{w}_{k,l}^{(2)}$  on plane  $\Pi_k$ .  $\mathbf{w}_{k,l}^{(1)}$  is placed on inner surface of intestine.  $\mathbf{w}_{k,l}^{(2)}$  is  $a_{13}$  [mm] distant from  $\mathbf{w}_{k,l}^{(1)}$ .

around the intestinal lumen on  $\Pi_k$  is calculated by

$$S_k = \frac{1}{L} \sum_{l=1}^L s_{k,l}. \quad (13)$$

The average CT value of the tissue around the intestinal lumen at  $\mathbf{p}_{\omega^i}$  is described as  $S_{\omega^i}$ . If it is smaller than  $a_{14}$  [H.U.], region  $c_i$  is removed in the reduction step.  $a_{14}$  [H.U.] is a threshold of the CT value of the tissue around the intestinal lumen.

#### 2.4.6 Reduction

We remove region  $c_i$  if the feature values of the region ( $r_i$ ,  $h_{\omega^i}$ , and  $S_{\omega^i}$ ) meet any of the following conditions:

$$r_i < a_{10}, \quad (14)$$

$$h_{\omega^i} > Ha_{11}, \quad (15)$$

$$S_{\omega^i} < a_{14}. \quad (16)$$

Next, we apply a dilation filter to the remaining regions. The structure element of the dilation filter is a sphere of radius  $a_{15}$  [mm]. The resulting regions of the dilation filter are defined as the final candidate regions.

### 3. Experiments

We applied our proposed method to ten cases of fecal tagging 3D abdominal CT images. Before taking the CT images, we confirmed the lesion position and injected an X-ray opaque contrast agent into the digestive fluid in the intestines with a fiber endoscope with insufflation of the intestines with air. Then the CT images were taken in a distended state. A medical doctor who is a specialist in gastroenterology checked the position of the ulcers carefully in the endoscopic and CT-based diagnoses. In the endoscopic diagnosis, almost all of the ulcers were found in the region where the endoscope reaches. Regions beyond the stenosed parts of the intestine were not observed by endoscope. The medical doctor also checked the remaining region of the intestine by careful observation of the CT images. Ulcers

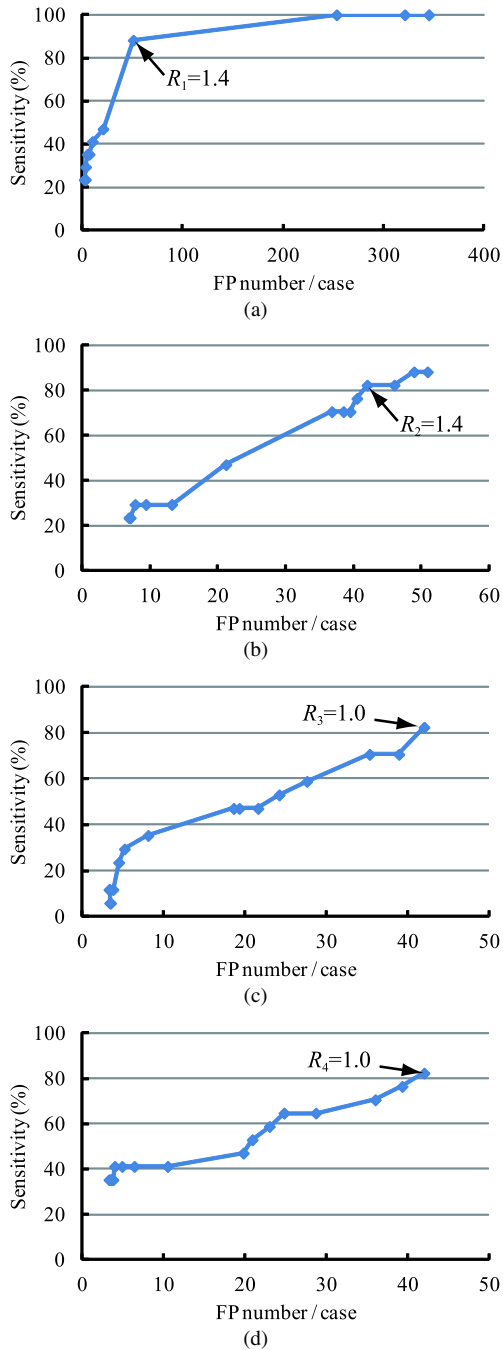


**Fig. 8** FROC curves obtained by changing parameters of FP reduction process. FROC curves with parameters: (a)  $R_1 = 1.0, \dots, 9.0, R_2 = 1.0, R_3 = 1.0, R_4 = 1.0, a_{11} = 10.0, a_{14} = -500$ , (b)  $R_1 = 1.4, R_2 = 1.0, \dots, 17.0, R_3 = 1.0, R_4 = 1.0, a_{11} = 10.0, a_{14} = -500$ , (c)  $R_1 = 1.4, R_2 = 1.4, R_3 = 1.0, \dots, 17.0, R_4 = 1.0, a_{11} = 10.0, a_{14} = -500$ , and (d)  $R_1 = 1.4, R_2 = 1.4, R_3 = 1.0, R_4 = 1.0, \dots, 17.0, a_{11} = 10.0, a_{14} = -500$ .

found from the endoscopic and CT-based diagnoses were defined as the gold standards of the experiments. 17 ulcers were found from these cases and used as gold standards. Endoscopic and CT-based diagnoses cause some false negatives (FNs) even when they were done by experts. Although our experiments utilized diagnostic results made by a medical specialist as gold standard, they might be insufficient.

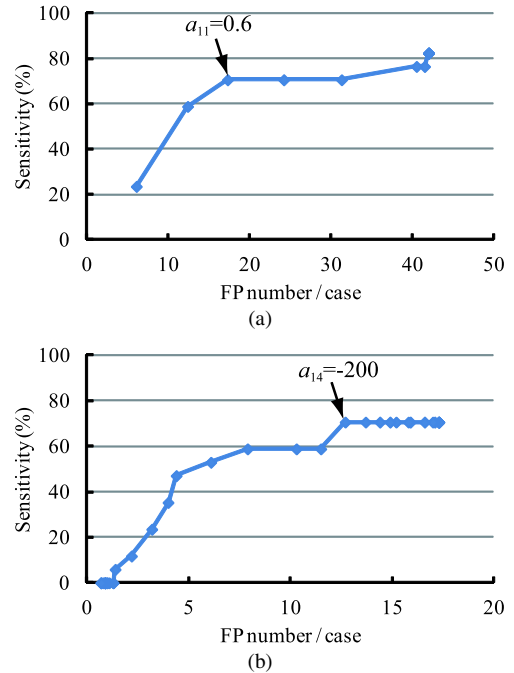


**Fig. 9** FROC curves obtained by changing parameters of FP reduction process. FROC curves with parameters: (a)  $R_1 = 1.4, R_2 = 1.4, R_3 = 1.0, R_4 = 1.0, a_{11} = 0.2, \dots, 10.0, a_{14} = -500$  and (b)  $R_1 = 1.4, R_2 = 1.4, R_3 = 1.0, R_4 = 1.0, a_{11} = 0.6, a_{14} = -500, \dots, 220$ .

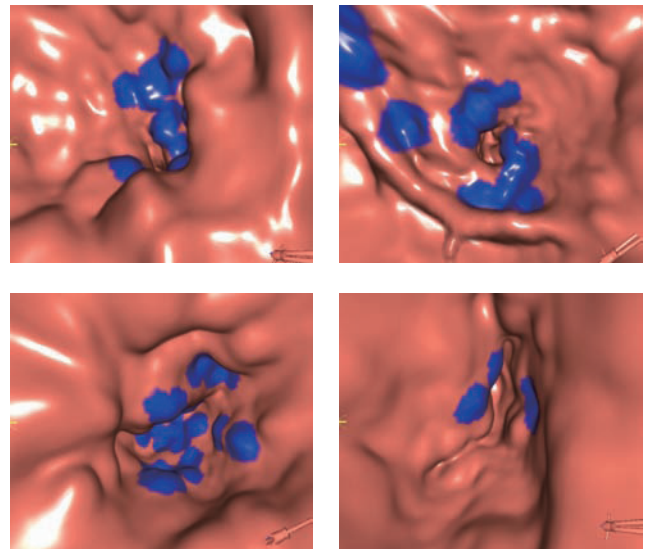
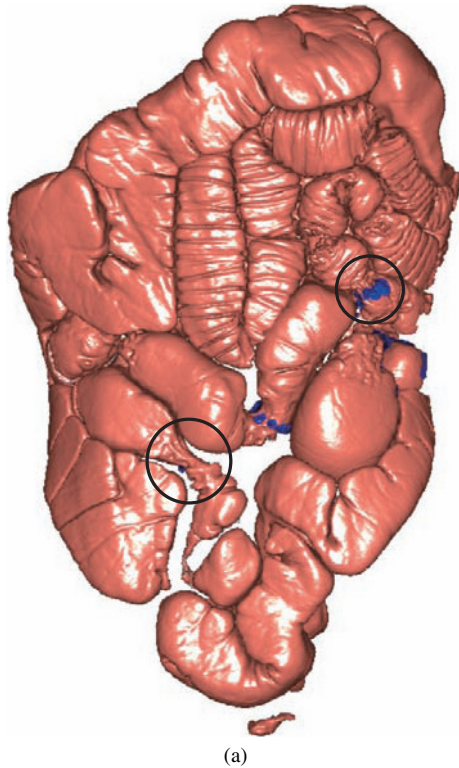
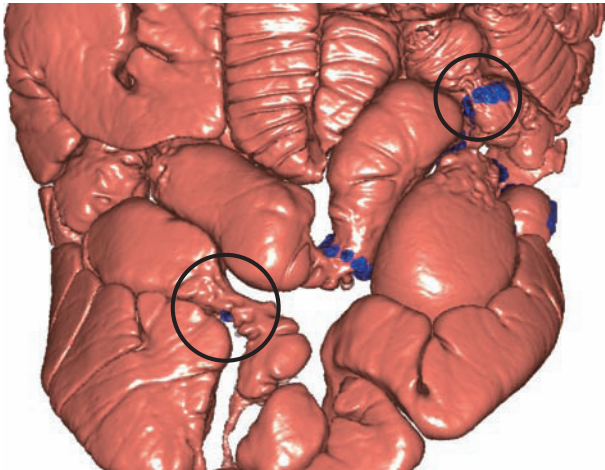


**Fig. 10** Detection results of ulcers by proposed method shown in virtual endoscopic views. Detected regions are marked by blue.

This is a limitation of this paper. The following are the acquisition parameters of the CT images: image size:  $512 \times 512$  [pixels], number of slices: 841-1051, pixel spacing: 0.55-0.67 [mm], slice spacing: 0.50 [mm], slice thickness: 0.50 [mm], tube voltage: 120 [kVp], and tube current: 138-387 [mAs]. The parameters used were set as  $a_1 = -650$  [H.U.],  $a_2 = 1000$  [mm<sup>3</sup>],  $a_3 = 1000$  [mm<sup>2</sup>],  $a_4 = 3.0$  [mm],  $a_5 = 5.0$  [mm],  $a_6 = 2.0, 3.0$  [mm],  $a_7 = 10$ ,  $a_8 = 70$ ,



(a)

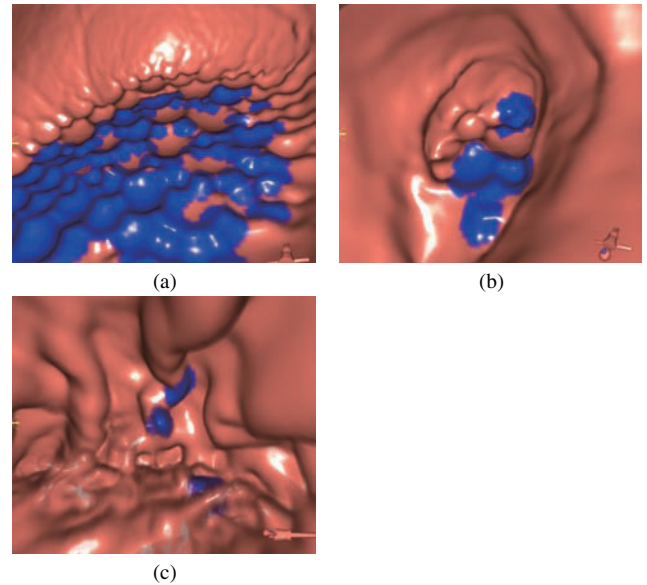


(b)

**Fig. 11** Detection results of ulcers by proposed method shown on intestine surface. These images are obtained by observing the intestine surface from its outside. Detected regions are marked by blue. Ulcer regions are indicated by circles. Narrowing of intestinal lumen regions occurs around the ulcers: (a) all intestines and (b) close-up of ulcers.

$a_9 = 190$ ,  $m = 1000$ ,  $n = 4$ ,  $a_{10} = 1$ ,  $L = 36$ ,  $a_{12} = -650$  [H.U.],  $a_{13} = 3.0$  [mm], and  $a_{15} = 3.0$  [mm]. These parameters were experimentally selected.

To determine the main parameters of the FP reduction process,  $R_1, R_2, R_3, R_4, a_{11}, a_{14}$ , we generated FROC curves by calculating the sensitivity and the FP number/case as varying FP reduction parameters. We obtained the optimal values of the FP reduction parameters as follows. First, we chose one parameter as a starting parameter to be optimized.



(a)

(b)

(c)

**Fig. 12** Examples of FPs of proposed method shown in virtual endoscopic views. Detected regions are marked by blue: (a), (b) bubbling fluid surface and (c) folds in stomach.

Then we drew a FROC curve by changing the parameter. We found a parameter that achieved at least 70% or higher sensitivity with the lower FPs in the detection result. The range and initial values of the FP reduction parameters affect this parameter optimization. They are defined by pre-investigating the feature value distributions. Initial values can be found as values that produce maximum sensitivity with the lowest number of FPs. In these initial values, of course, many FP regions were generated in this setting. The ranges of the parameters were also determined from the distributions of the feature values.

Figure 8 (a) shows a FROC curve obtained by setting the parameters to  $R_1 = 1.0, \dots, 9.0, R_2 = 1.0, R_3 = 1.0, R_4 = 1.0, a_{11} = 10.0$ , and  $a_{14} = -500$ . From the FROC curve, the sensitivity was 88.2% (15/17) with 50.9 FPs/case when  $R_1 = 1.4$ . Similarly, from the FROC curve shown in Fig. 8 (b), the sensitivity was 82.4% (14/17) with 42.0 FPs/case when  $R_2 = 1.4$ . From the FROC curve shown in Figs. 8 (c) and (d), the sensitivity was 82.4% (14/17) with 42.0 FPs/case when  $R_3 = 1.0, R_4 = 1.0$ . We set the values to the coefficient of the radius of the intestines as  $a_{11} = 0.2, \dots, 10.0$  to obtain the FROC curve shown in Fig. 9 (a). The sensitivity was 70.6% (12/17) with 17.3 FPs/case when  $a_{11} = 0.6$ . We set the values to the threshold of the CT value of the tissue around the intestinal lumen as  $a_{14} = -500, \dots, 220$  to obtain the FROC curve shown in Fig. 9 (b). From this curve, the sensitivity was 70.6% (12/17) with 12.7 FPs/case when  $a_{14} = -200$ .

Figures 10, 11, and 12 show the ulcers and the FPs detected by our proposed method. Many convex and concave regions were detected on the ulcers. The detected regions are shown by blue. The false positives included a bubbling fluid surface and folds in the stomach. Figure 13 shows examples of the FNs of the proposed method. The proposed

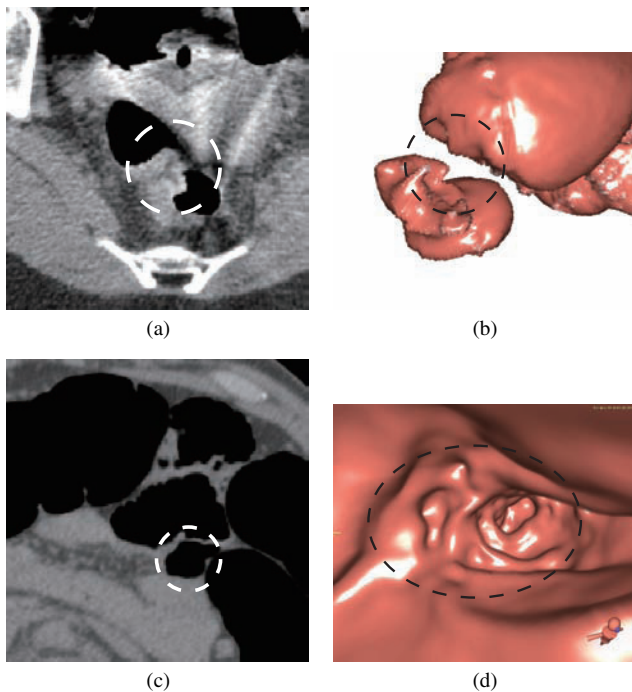


**Fig. 13** Examples of FNs: (a) slice image and (b) surface of intestine of ulcer causing completely stenosed intestine. Stenosed regions are indicated by circles; (c) slice and (d) virtual endoscopic images of ulcer on thin intestinal wall. Ulcer regions are indicated by circles.

method could not find ulcer causing a completely stenosed intestine and ulcer on a thin intestinal wall.

#### 4. Discussion

Since an ulcer is an inflammatory disease, the ulcer regions consist of a number of convex and concave regions. Although their detection is very different from that of colonic polyps, the proposed method was able to detect the ulcer regions at reasonable sensitivity and FPs.

Our method, which detected 70.6% of ulcers with 12.7 FPs/case, also detected nine ulcer regions that were overlooked by endoscopic diagnosis. The proposed method effectively assists medical doctors find ulcers. The number of FPs/case is also acceptable for medical use for the following reason. CAD systems having the proposed method will be utilized as a supporting tool of optical endoscopy for cases where additional diagnosis is required due to the difficulty of endoscopy. In cases of stenosis, since an endoscope cannot pass through the stenosis part of the intestine, it is impossible to observe the area beyond the stenosis part. This creates non-observed regions of the intestine. In such cases, CT images are taken after optical endoscopy. CAD systems having our proposed method will be utilized to observe the regions where the endoscope cannot go through. Such complementary use of optical endoscopes and CAD based on CT images will explore a new diagnostic method. The combination of the two modalities will enable physicians to diagnose the entire area of the intestine when optical endoscopy cannot be completely performed. Patients under

suspicion of having Crohn's disease are found by such examinations as blood tests. Diagnoses by optical endoscope and CAD system are also performed on patients who might have Crohn's disease. For such patients, we must find as many ulcer regions as possible by combining optical endoscope and CAD-based diagnoses even if many FPs are caused. The 12.7 FPs/cases is acceptable for medical doctors. Reducing FNs is more important than reducing FPs.

Our proposed method detected the convex and concave regions of the ulcers on the intestinal wall (Fig. 10). BSE and iBSE filters detected them with high sensitivity. However, the results of the detection process include many FPs. We applied a FP reduction process using thresholding based on voxel values and the maximum voxel values of connected components; this removed many small FPs. However, since the results of the FP reduction process still included FPs, we used the roughness values for further FP reduction. Many convex and concave regions are concentrated in the local region on the ulcer surface. We utilized this shape characteristic of the ulcer. The roughness value measures the positional correspondences of the detected convex and concave regions. The FP reduction process using roughness values greatly reduced the number of FPs from 345.0 to 42.0 per case (Fig. 8). Additionally, we utilized the shape and the CT value characteristics of the intestines for FP reduction. The FP reduction processes based on the thickness of the intestinal lumen and the CT values of the surrounding tissue of the intestinal lumen reduced the number of FPs from 42.0 to 12.7 per case (Fig. 9). These feature values were effective for classifying the convex and concave candidate regions into true positives and FPs. However, further reduction of FPs is required for application of this method to the CAD of Crohn's disease. Further reduction is also required to efficiently diagnose ulcers using a CAD system with automated ulcer detection. The statistical position and shape analyses of ulcers may provide usable information for FP reduction. To perform the analyses, a large number of CT images including ulcers must be collected.

Our proposed method detected bubbles on the surface of the residue fluid in the intestines (Figs. 12 (a) and (b)) as many small convex and concave regions in the CT images. This shape characteristic resembles the surface of ulcers. Therefore, the bubbles were detected by our proposed method, which applies an electronic cleansing process to remove the tagged fluid in the intestines since we injected contrast agents into the fluid in the intestine using a fiber endoscope, we cannot inject contrast agents into the fluid beyond some stenosed parts of the intestines. The CT values of the fluid that contains no contrast agent resemble those of the intestinal wall. Therefore, the electronic cleansing process cannot remove the non-contrasted fluid. To reduce the FPs caused by the bubbles on the non-contrasted fluid, we must modify the administration method of the contrast agents.

The FN results of the proposed method were an ulcer causing a completely stenosed intestine and an ulcer on the thin intestinal wall (Fig. 13). They were missed because their shapes were different from our assumption of the shape

of ulcers. The ulcer causing the completely stenosed intestine (Fig. 13 (a) and (b)) divided the air region in the intestine into two regions by stenosis. We assume an ulcer is located in an air region. Based on this assumption, the roughness value evaluates how the candidate regions are concentrated in air regions. However, the separation of the air region by stenosis decreased the roughness value and caused the false removal of candidate regions. To reduce FNs around the completely stenosed parts, we must not only detect the ulcer regions of its surface but also the tissues inside. Another example of FN is an ulcer on a thin intestinal wall, as shown in Fig. 13 (c) and (d). We utilized the CT values of the surrounding tissues of the intestinal lumen as a feature value of the FP reduction process. We assume a thick intestinal wall at the ulcer and high CT values. However, the thickness of the intestinal wall decreases if too much air is insufflated to the intestine. The condition of the air insufflation to the intestine must be considered in the FP reduction process based on the thickness of the intestinal wall.

We found FP reduction parameters by a manual optimization process. FP reduction is done by a combination of thresholding processes. This will not cause severe over-training. Therefore, we used the same set of CT images in the parameter tuning and evaluation. To automate the parameter tuning process, we will reduce FPs by a machine learning approach. Clear separation of learning and testing data will be performed.

## 5. Conclusions

This paper proposed an automated detection method of the convex and concave regions on ulcers in the small and large intestines from fecal tagging CT images. Ulcers cause many convex and concave regions on the intestinal wall. Our proposed method detects them using blob and inverse-blob structure enhancement filters. The FPs of the detection results are removed utilizing roughness values. The convex and concave regions on the ulcers are locally concentrated. The roughness value evaluates their concentration ratios to remove the FPs using their positional correspondences. The thickness of the intestinal lumen and the CT values of the surrounding tissue of the intestinal lumen are also used as feature values of FP reduction. We applied our proposed method to ten cases of fecal tagging CT images and detected 70.6% of the ulcers with 12.7 FPs/case. Future work includes further reduction of FPs and FNs, development of an estimation method of the ulcer region from the detection results, and application of it to a CAD system for Crohn's disease.

## Acknowledgements

The authors thank our colleagues for suggestions and advice. Parts of this research were supported by a Grant-in-Aid for Scientific Research from the Ministry of Education (MEXT), the Japan Society for the Promotion of Science (JSPS), the Fund for Cancer Research and Develop-

ment from the National Cancer Center, and the Kayamori Foundation of Informational Science Advancement.

## References

- [1] K. Asakura, Y. Nishiwaki, N. Inoue, T. Hibi, M. Watanabe, and T. Takebayashi, "Prevalence of ulcerative colitis and Crohn's disease in Japan," *J. Gastroenterology*, vol.44, no.7, pp.659–665, May 2009.
- [2] T. Yao, T. Matsui, and N. Hiwatashi, "Crohn's disease in Japan: diagnostic criteria and epidemiology," *Diseases of The Colon & Rectum*, vol.43, sup.10, pp.S85–S93, Oct. 2000.
- [3] Z. Fireman, E. Mahajna, E. Broide, M. Shapiro, L. Fich, A. Sternberg, Y. Kopelman, and E. Scapa, "Diagnosing small bowel Crohn's disease with wireless capsule endoscopy," *An Int. J Gastroenterology and Hepatology*, vol.52, no.3, pp.390–392, March 2003.
- [4] S.L. Triester, J.A. Leighton, G.I. Leontiadis, S.R. Gurudu, D.E. Fleischer, A.K. Hara, R.I. Heigh, A.D. Schiff, and V.K. Sharma, "A meta-analysis of the yield of capsule endoscopy compared to other diagnostic modalities in patients with non-stricturing small bowel Crohn's disease," *American Journal of Gastroenterology*, vol.101, no.5, pp.954–964, May 2006.
- [5] S.S. Lee, A.Y. Kim, S.-K. Yang, J.-W. Chung, S.Y. Kim, S.H. Park, and H.K. Ha, "Crohn disease of the small bowel: comparison of CT enterography, MR enterography, and small-bowel follow-through as diagnostic techniques," *Radiology*, vol.251, no.3, pp.751–761, June 2009.
- [6] A. Furukawa, T. Saotome, M. Yamasaki, K. Maeda, N. Nitta, M. Takahashi, T. Tsujikawa, Y. Fujiyama, K. Murata, and T. Sakamoto, "Cross-sectional imaging in Crohn disease," *RadioGraphics*, vol.24, no.3, pp.689–702, May 2004.
- [7] J.R. Leyendecker, R.S. Bloomfield, D.J. DiSantis, G.S. Waters, R. Mott, and R.E. Bechtold, "MR enterography in the management of patients with Crohn disease," *RadioGraphics*, vol.29, no.6, pp.1827–1846, Oct. 2009.
- [8] H.A. Siddiki, J.L. Fidler, J.G. Fletcher, S.S. Burton, J.E. Huprich, D.M. Hough, C.D. Johnson, D.H. Bruining, E.V. Loftus, W.J. Sandborn, D.S. Pardi, and J.N. Mandrekar, "Prospective comparison of state-of-the-art MR enterography and CT enterography in small-bowel Crohn's disease," *American Journal of Roentgenology*, vol.193, no.1, pp.113–121, July 2009.
- [9] J.A.W. Tielbeek, F.M. Vos, and J. Stoker, "A computer-assisted model for detection of MRI signs for Crohn's disease activity: future or fiction?," *Abdominal Imaging*, vol.37, no.6, pp.967–973, Dec. 2012.
- [10] S.R. Paulsen, E. Huprich, G. Fletcher, F. Booya, B.M. Young, L. Fidler, D. Johnson, M. Barlow, and F. Earnest IV, "CT enterography as a diagnostic tool in evaluating small bowel disorders: review of clinical experience with over 700 cases," *RadioGraphics*, vol.26, no.3, pp.641–662, May 2006.
- [11] F. Booya, S. Akram, J.G. Fletcher, J.E. Huprich, C.D. Johnson, J.L. Fidler, J.M. Barlow, C.A. Solem, W.J. Sandborn, and E.V. Loftus Jr., "CT enterography and fistulizing Crohn's disease: clinical benefit and radiographic findings," *Abdominal Imaging*, vol.34, no.4, pp.467–475, July 2009.
- [12] A.K. Hara, S. Alam, R.I. Heigh, S.R. Gurudu, J.G. Hentz, and J.A. Leighton, "Using CT enterography to monitor Crohn's disease activity: a preliminary study," *American Journal of Roentgenology*, vol.190, no.6, pp.1512–1516, June 2008.
- [13] Y. Ota, T. Matsui, H. Ono, H. Uno, H. Mataka, S. Tsuda, T. Sakurai, and T. Yao, "Value of virtual computed tomographic colonography for Crohn's colitis: comparison with endoscopy and barium enema," *Abdominal Imaging*, vol.28, no.6, pp.778–783, Nov. 2003.
- [14] L. Biancone, R. Fiori, C. Tosti, A. Marinetti, M. Catarinacci, F.D. Nigris, G. Simonetti, and F. Pallone, "Virtual colonoscopy compared with conventional colonoscopy for stricturing postoperative

recurrence in Crohn's disease," *Inflammatory Bowel Diseases*, vol.9, no.6, pp.343–350, 2003.

- [15] J. Nappi and H. Yoshida, "Adaptive correction of the pseudo-enhancement of CT attenuation for fecal-tagging CT colonography," *Medical Image Analysis*, vol.12, no.4, pp.413–426, Jan. 2008.
- [16] M. Oda, T. Kitasaka, K. Mori, Y. Suenaga, T. Takayama, H. Takabatake, M. Mori, H. Natori, and S. Nawano, "Digital bowel cleansing free colonic polyp detection method for fecal tagging CT colonography," *Academic Radiology*, vol.16, no.4, pp.486–494, 2009.
- [17] M. Oda, K. Furukawa, O. Watanabe, T. Ando, H. Goto, and K. Mori, "Detection of ulcers based on roughness value from fecal tagging CT image," *Int. J CARS*, pp.S200–S202, June 2011.
- [18] M. Oda, T. Kitasaka, K. Mori, K. Furukawa, O. Watanabe, T. Ando, and H. Goto, "Development of CAD prototype system for Crohn's disease," *Proc. SPIE Medical Imaging*, vol.7624, pp.76241U-1–10, Feb. 2010.



**Masahiro Oda** received the B.S. degree in Information Engineering and the M.S. and the Ph.D. degrees in Information Science from Nagoya University, Japan, in 2004, 2006, and 2009. He was a postdoctoral fellow of Nagoya University, Japan in 2009–11. Since 2011, he has been an Assistant Professor at Graduate School of Information Science, Nagoya University, Japan. His current research interests include medical image processing and pattern recognition. He received the RSNA 2009 Certificate of Merit, the student award of the Institute of Electronics, Information, and Communication Engineers Tokai-Section in 2007, and the incentive award of the Tokai-Section Joint Conference on Electrical and Related Engineering in 2005. He is a member of the Japan Society of Medical Imaging Technology, and the Japan Society of Computer Aided Surgery.



**Takayuki Kitasaka** received the B.S. degree in Information Engineering and the Ph.D. degree in Engineering from Nagoya University, Japan, in 1997 and 2002. He was an Assistant Professor of School of Engineering, Nagoya University in 2003–08. He was a Lecturer of Aichi Institute of Technology in 2008–11. Since 2011, he has been an Associate Professor of Aichi Institute of Technology. His current research interest is pattern recognition of human body images. He is a member of the Japanese

Society of Medical Imaging Technology, and the Japan Society of Computer Aided Surgery.



**Kazuhiro Furukawa** received the M.D. degree from Nagoya University School of Medicine, Japan, in 2000 and the Ph.D. degree from Nagoya University Graduate School of Medicine in 2011. He is an attending staff of Department of Gastroenterology and Hepatology, Nagoya University Graduate School of Medicine. He is a Board Certified Member of the Japanese Society of Internal Medicine, Board Certified Gastroenterologist of the Japanese Society of Gastroenterology, Board

Certified Fellow of the Japan Gastroenterological Endoscopy Society, General Clinical Oncologist by Japanese Board of Cancer Therapy, Board Certified Specialist of the Japanese Society of Gastroenterological Cancer Screening, and Occupational Physician Certified by Japan Medical Association.



**Osamu Watanabe** received the M.D. degree in Nagoya University School of Medicine, Japan, in 1993 and the Ph.D. degree in Nagoya Graduate School of Medicine in 2009. He was a research scholar in 2002–2007. Since 2008, he has been an Assistant Professor at Nagoya University Hospital, Nagoya, Japan. He conducts clinical researches on inflammatory bowel diseases. He is a member of the Japanese Society of Internal Medicine, and the Japanese Society of Gastroenterology, and the Japan Gas-

tronterological Endoscopy Society.



**Takafumi Ando** received the M.D. degree from Jichi Medical University, in 1983 and the Ph.D. degree from Nagoya University, Japan in 1996. He was a Medical Staff in several hospitals in 1983–1992. He was a Medical Staff in Internal Medicine, Nagoya University school of Medicine, Japan in 1993–1997. He was a Visiting Scholar of Vanderbilt University Medical Center, Nashville, TN, USA in 1997–2000. He was a Postdoctoral fellow in Medicine, New York University Medical Center, New York, NY,

USA in 2000–1. He was a Medical Staff in Internal Medicine, Nagoya University school of Medicine, Japan in 2001–4. He was an Associate Professor, Department of Gastroenterology, Nagoya University Graduate School of Medicine, Japan in 2004–7. Since 2007, he has been an Associate Professor, Department of Gastroenterology, Nagoya University Graduate School of Medicine, Japan. His current research interests include diagnosis and assessment of inflammatory bowel diseases. He is a member of the American Gastroenterological Association and Japanese Society of Gastroenterology.



**Hidemi Goto** received the M.D. degree from School of Medicine, Nagoya University in 1979. He was Associate Professor of Department of Endoscopy, Nagoya University Hospital in 1999–2003. Since 2003, he has been Professor and Chairman of Department of Gastroenterology and Hepatology, Nagoya University Graduate School of Medicine. He has been a Vice President of Nagoya University Hospital from 2007. His research interests are developing diagnostic methods and endoscopic treatments

for cancers of digestive organs. He is a Board Certified Member and an attending physician of the Japanese Society of Internal Medicine, an attending physician of the Japanese Society of Gastroenterology, and more. He is President of Tokai Branch of the Japanese Society of Gastroenterology, a councilor of the Japan Gastroenterological Endoscopy Society, and more.



**Kensaku Mori** received the B.S degree in electronics engineering, the M.S degree in information engineering, and the Ph.D. in information engineering from Nagoya University, Japan, in 1992, 1994 and 1996, respectively. He was a research fellow of the Japanese Society for the Promotion of Science (JSPS) from 1994 to 1997, a Research Associate at Department of Computational Science and Engineering, Nagoya University from 1997 to 2000, an Assistant Professor in 2000. He was an Associate Professor at the Research Center for Advance Waste and Emission

Management of Nagoya University from 2001 to 2003. He was also a Visiting Associate Professor at Department of Neurosurgery, Stanford University, U.S.A., from 2001 to 2002. He was an Associate Professor of the Graduate School of Information Science, Nagoya University from 2003 to 2009. He has been a Professor of Information and Communications Headquarters, Nagoya University since 2009. His current research interests include three dimensional image processing, computer graphics, virtual reality and their applications to medical image. He has received many awards from several institutes including the Young Researcher Award, Ministry of Education, Culture, Sports, the Best Paper Awards from the Japanese Society of Medical Imaging Technology. He is appointed as the General Chair of the 16th International Conference of Medical Image Computing and Computer Assisted Intervention (MICCAI 2013). He is a member of Japanese Society of Biomedical Engineering, and Japanese Society of Medical Imaging Technology, MICCAI, IEEE, and SPIE.